 Inorg. Chem. **2009,** *48,* 4882–4895
DOI:10.1021/ic900274a

Inorganic Chemistry
Article

Structural and Photoluminescence Studies of a Europium(III) Tetrakis (β-diketonate) Complex with Tetrabutylammonium, Imidazolium, Pyridinium and Silica-Supported Imidazolium Counterions

Sofia M. Bruno,[†] Rute A. S. Ferreira,[‡] Filipe A. Almeida Paz,[†] Luís D. Carlos,*[,‡] Martyn Pillinger,[†] Paulo Ribeiro-Claro,[†] and Isabel S. Gonçalves*[,†]

[†]*Department of Chemistry, CICECO, University of Aveiro, 3810-193 Aveiro, Portugal, and* [‡]*Department of Physics, CICECO, University of Aveiro, 3810-193 Aveiro, Portugal*

Received February 10, 2009

Tetrakis(naphthoyltrifluoroacetonato)lanthanate(III) complexes (Ln = Eu, Gd) containing the cations tetrabutylammonium, $[NBu_4]^+$; 1-butyl-3-methylimidazolium, $[C_4mim]^+$; and 1-butyl-3-methylpyridinium, $[C_4mpyr]^+$, have been prepared and structurally characterized by single-crystal X-ray diffraction. The $\{EuO_8\}$ coordination sphere in $[NBu_4][Eu(NTA)_4]$ is best described as a distorted dodecahedron, where the metal ion is located at the 4-fold inversion axis with only one crystallographically independent NTA residue. In $[C_4mim][Eu(NTA)_4]$ and $[C_4mpyr][Gd(NTA)_4]$, the central Ln^{3+} ions are coordinated by eight oxygen atoms from four distinct β-diketonate ligands, in an overall distorted square-antiprismatic geometry. Besides electrostatic interactions, the crystal packing in all three structures is stabilized by offset $\pi-\pi$ interactions involving the naphthyl rings of neighboring complexes (and, for $[C_4mim][Eu(NTA)_4]$ and $[C_4mpyr][Gd(NTA)_4]$, neighboring naphthyl/imidazolium and naphthyl/pyridinium rings) and $C-H\cdots\pi$ contacts. The photoluminescence properties of the three Eu^{III} complexes were studied at room temperature and -259 °C by measuring emission and excitation spectra, $^5D_0$ emission decay curves, and absolute emission quantum yields. Under ligand excitation (λ_{ex} = 290−395 nm), the quantum yields (room temperature) were in the range 0.72−0.77 for the 1-butyl-3-methylimidazolium salt. An immobilized analogue of this complex was prepared by supporting $[Eu(NTA)_4]^-$ on an ordered mesoporous silica derivatized with 1-propyl-3-methylimidazolium groups. The disappearance of the intra-$4f^6$ lines in the excitation spectrum of the supported material indicated an increase in the ligand's sensitization process of the Eu^{3+} ions, relative to direct intra-$4f^6$ excitation. The emission quantum yield measured for the supported material (0.32−0.40, for excitations between 265 and 360 nm) is the highest so far reported for lanthanide-containing ordered mesoporous silicas.

Introduction

During the past 40 years, there has been considerable interest in the luminescence and lasing ability of lanthanide (Ln) complexes bearing β-diketone (diket) ligands.[1] One major goal is the synthesis of stable compounds that can function as efficient light conversion molecular devices. By introduction of chromophoric groups in the ligands, an intense luminescence of the metal ion can be obtained via the "antenna effect", that is, energy transfer from the absorbing organic component to the emitting central ion.[1,2] Most of the complexes investigated emit red or green light (Eu^{3+} and Tb^{3+} luminescence, respectively), but there are also complexes of other Ln^{3+} ions that exhibit luminescence in other spectral regions, such as near-IR (Yb^{3+}, Nd^{3+}, Er^{3+}). Two classes of complexes may be distinguished depending on whether the ratio of diketonate ions to metal ions in the product is 3:1 (triscomplex) or 4:1 (tetrakiscomplex). The luminescence efficiency of the β-diketonate complexes can be increased by an appropriate choice of substituents on the β-diketone ligand, because in this way the position of the ligand's triplet level can be tuned to give good energy transfer between the β-diketone ligand and the lanthanide ion. A combination of aromatic and fluorinated alkyl groups tends to give the best results. The presence of C−F bonds, as opposed to C−H, a higher-energy frequency oscillator, helps reduce nonradiative quenching of lanthanide luminescence.

*Authors to whom correspondence should be addressed. E-mail: igoncalves@ua.pt (I.S.G.) and lcarlos@ua.pt (L.D.C.).

(1) (a) Binnemans, K. Rare-Earth Beta-Diketonates. In *Handbook on the Physics and Chemistry of Rare Earths*; Gschneidner, K. A., Jr., Bünzli, J.-C. G., Pecharsky, V. K., Eds.; Elsevier: Amsterdam, **2005**; Vol. *35*, Chapter 225, pp 107−272. (b) Carlos, L. D.; Ferreira, R. A. S.; de Zea Bermudez, V.; Ribeiro, S. J. L. *Adv. Mater.* **2009**, *21*, 509–534. (c) Lis, S.; Elbanowski, M.; Mąkowska, B.; Hnatejko, Z. *J. Photochem. Photobiol. A: Chem.* **2002**, *150*, 233–247. (d) de Sá, G. F.; Malta, O. L.; de Mello Donegá, C.; Simas, A. M.; Longo, R. L.; Santa-Cruz, P. A.; da Silva, E. R., Jr. *Coord. Chem. Rev.* **2000**, *196*, 165–195.

(2) Bünzli, J.-C. G.; Piguet, C. *Chem. Soc. Rev.* **2005**, *34*, 1048–1077.

 Published on Web 4/20/2009

In the case of tetrakis(β-diketonate) complexes, (C)[Ln(diket)$_4$], additional tuning of the photophysical properties is possible by changing the counterion, C^+, which changes the structure of the complex, in particular the local coordination geometry of the metal ion.[3]

Some recent publications have focused on the combination of ionic liquids (ILs) with lanthanide tetrakis(β-diketonate) complexes for spectroscopic applications.[4−7] ILs are salts with a melting point below 100 °C.[8] The cation of an IL is usually a large organic cation, such as imidazolium, pyridinium, or quaternary ammonium ions, and the anion can be an inorganic or small organic anion like halides, BF_4^-, PF_6^-, $CF_3SO_3^-$ (TfO), and $(CF_3SO_2)_2N^-$ (Tf_2N). Imidazolium ILs containing the 1-alkyl-3-methylimidazolium cation, abbreviated as $[C_n\text{mim}]^+$, are the most popular. In the study by Driesen et al.,[4] intense NIR luminescence was observed upon ligand excitation for $[Nd(NTA)_4]^-$ complexes (HNTA = 1-(2-naphthoyl)-3,3,3-trifluoroacetone) dissolved in [C_6mim]Br. Nockemann et al. found that the photostability of the 1-hexyl-3-methylimidazolium tetrakis(2-thenoyltrifluoroacetonato)europate(III) complex, [C_6mim][Eu(TTA)$_4$], was enhanced after dissolving the complex in a weakly coordinating imidazolium IL.[5] By introducing the $[C_6\text{mim}]^+$ cation in the ionic complex, the solubility in the corresponding IL, [C_6mim][Tf_2N], was improved. Two very recent lines of research demonstrate the potential of these systems to be developed as laser dyes or as luminescent materials for emissive displays and light-converting devices.[6,7] In the first example, a luminescent ionic liquid crystal was prepared by attaching two mesogenic cholesterol groups to an imidazolium core and combining the resultant cation with an $[Eu(TTA)_4]^-$ anion.[6] In the second example, luminescent ionogels were prepared by doping the complexes [C_6mim][Eu(NTA)$_4$] and [C_6mim][Ln(TTA)$_4$] (Ln = Nd, Sm, Eu, Ho, Er, Yb) into the IL [C_6mim][Tf_2N], followed by immobilization of the IL by confinement in a silica network.[7]

The references cited above show that the design of complexes containing imidazolium, pyridinium, or quaternary ammonium ions, and $[Ln(diket)_4]^-$ anions, is an important step in the synthesis of luminescent materials containing lanthanides and ILs. In the present work, tetrakis(naphthoyltrifluoroacetonato)lanthanate(III) complexes (Ln = Eu, Gd) containing the cations tetrabutylammonium, $[NBu_4]^+$; 1-butyl-3-methylimidazolium, $[C_4\text{mim}]^+$; and 1-butyl-3-methylpyridinium, $[C_4\text{mpyr}]^+$, have been prepared and their photoluminescence properties studied. Naphthoyltrifluoroacetone was chosen as the β-diketone ligand because it is known to be a very efficient sensitizer of europium(III)-centered luminescence.[1a,9] The X-ray crystal structures of three of the compounds are described. An immobilized analogue of the complex [C_4mim][Eu(NTA)$_4$] was prepared by using the ordered mesoporous silica MCM-41 derivatized with 1-propyl-3-methylimidazolium groups as a support for the $[Eu(NTA)_4]^-$ anion.

Experimental Section

Characterization Methods. Microanalyses for CHN and inductively coupled plasma−atomic emission spectrometry determination of Eu were performed at the University of Aveiro. Thermogravimetric analysis (TGA) and differential scanning calorimetry (DSC) were carried out under air using Shimadzu TGA-50 and DSC-50 systems, with a heating rate of 5 °C min^{-1}. Powder XRD data were collected on an X'Pert MPD Philips diffractometer (Cu K_α X-radiation, λ = 1.54060 Å) fitted with a graphite monochromator and a flat plate sample holder, in a Bragg−Brentano para-focusing optics configuration (40 kV, 50 mA). Samples were step-scanned in 0.02° 2θ steps with a counting time of 2 s per step. FTIR spectra were obtained on a FTIR Mattson-7000 infrared spectrophotometer with 2 cm^{-1} resolution, using KBr pellets. FT Raman spectra were recorded on an RFS-100/S Bruker FT spectrometer, using a Nd:YAG laser (Coherent compass-1064/500) with an excitation wavelength of 1064 nm and a 2 cm^{-1} resolution. Solid-state magic-angle spinning (MAS) NMR spectra were recorded at 79.49 MHz for ^{29}Si and 125.76 MHz for ^{13}C on Bruker Avance 400/500 spectrometers. ^{29}Si MAS NMR spectra were recorded with 40° pulses, spinning rates of 5.0 kHz, and 60 s recycle delays. ^{29}Si cross-polarization (CP) MAS NMR spectra were recorded with 4.0 μs ^{1}H 90° pulses, a contact time of 8 ms, a spinning rate of 5 kHz, and 5 s recycle delays. ^{13}C CP MAS NMR spectra were recorded with 4.5 μs ^{1}H 90° pulses, a contact time of 2 ms, a spinning rate of 7.0 kHz, and 4 s recycle delays. Solution NMR spectra were measured using a Bruker CXP 300 spectrometer for ^{1}H and a Bruker Avance 500 Cryo ultrashield spectrometer for ^{13}C (University of Cambridge). Chemical shifts are quoted in parts per million from tetramethylsilane.

The photoluminescence and lifetime measurements were made between −259 and +155 °C on a Fluorolog-3 model FL3-2T spectrometer with double excitation, fitted with a 1200 grooves/mm grating blazed at 330 nm, and a TRIAX 320 single emission spectrometer coupled to a R928 photomultiplier, fitted with a 1200 grooves/mm grating blazed at 500 nm. The temperature variation between 26 and 155 °C was achieved using an IES-RD31 controller and a Kapton thermofoil heater from Minco, mounted on a Cu holder. The excitation sources were a 450 W Xe arc lamp and a pulsed Xe−Hg lamp for the steady-state and time-resolved measurements, respectively. Excitation spectra were corrected from 240 to 600 nm for the spectral distribution of the lamp intensity using a photodiode reference detector. Emission spectra were also corrected for the spectral response of the monochromators and the detector using typical correction spectra provided by the manufacturer. The absolute emission quantum yields were measured at room temperature using a Quantum Yield Measurement System C9920-02 from Hamamatsu with a 150 W xenon lamp coupled to a monochromator for wavelength discrimination, an integrating sphere as a sample chamber, and a multichannel analyzer for signal detection. The experimental error is within 10%.

(3) Mech, A.; Karbowiak, M.; Görller-Walrand, C.; Van Deun, R. *J. Alloys Compd.* **2008**, *451*, 215–219.
(4) Driesen, K.; Nockemann, P.; Binnemans, K. *Chem. Phys. Lett.* **2004**, *395*, 306–310.
(5) Nockemann, P.; Beurer, E.; Driesen, K.; Deun, R. V.; Hecke, K. V.; Meervelt, L. V.; Binnemans, K. *Chem. Commun.* **2005**, 4354–4356.
(6) Goossens, K.; Nockemann, P.; Driesen, K.; Goderis, B.; Görller-Walrand, C.; Hecke, K. V.; Meervelt, L. V.; Pouzet, E.; Binnemans, K.; Cardinaels, T. *Chem. Mater.* **2008**, *20*, 157–168.
(7) (a) Lunstroot, K.; Driesen, K.; Nockemann, P.; Görller-Walrand, C.; Binnemans, K.; Bellayer, S.; Bideau, J. L.; Vioux, A. *Chem. Mater.* **2006**, *18*, 5711–5715. (b) Lunstroot, K.; Driesen, K.; Nockemann, P.; Van Hecke, K.; Van Meervelt, L.; Görller-Walrand, C.; Binnemans, K.; Bellayer, S.; Viau, L.; Bideau, J. L.; Vioux, A. *Dalton Trans.* **2009**, 298–306.
(8) (a) Holbrey, J. D.; Seddon, K. R. *Clean Prod. Proc.* **1999**, *1*, 223–236. (b) Wasserscheid, P.; Keim, W. *Angew. Chem., Int. Ed.* **2000**, *39*, 3772–3789. (c) Welton, T. *Coord. Chem. Rev.* **2004**, *248*, 2459–2477.
(9) (a) Gago, S.; Fernandes, J. A.; Rainho, J. P.; Ferreira, R. A. S.; Pillinger, M.; Valente, A. A.; Santos, T. M.; Carlos, L. D.; Ribeiro-Claro, P. J. A.; Gonçalves, I. S. *Chem. Mater.* **2005**, *17*, 5077–5084. (b) Bruno, S. M.; Coelho, A. C.; Ferreira, R. A. S.; Carlos, L. D.; Pillinger, M.; Valente, A. A.; Ribeiro-Claro, P.; Gonçalves, I. S. *Eur. J. Inorg. Chem.* **2008**, 3786–3795. (c) Bruno, S. M.; Ferreira, R. A. S.; Carlos, L. D.; Pillinger, M.; Ribeiro-Claro, P.; Gonçalves, I. S. *Microporous Mesoporous Mater.* **2008**, *113*, 453–462.

Three measurements were performed for each sample and excitation wavelength, and the average value is presented.

Synthetic Procedures. Where appropriate, standard Schlenk techniques under nitrogen were used. Reagents were purchased from commercial sources and used as received. Solvents were dried by standard procedures, distilled under nitrogen, and kept over 4Å molecular sieves. 1-(3-Trimethoxysilyl)-propyl-3-methylimidazolium chloride was prepared by coupling 1-methylimidazole with (3-chloropropyl)trimethoxysilane.[10] ^{1}H and ^{13}C NMR data ($CDCl_3$) were in agreement with the results reported by Sasaki et al.[10] Purely siliceous MCM-41 was synthesized as described previously using $[CH_3(CH_2)_{13}N(CH_3)_3]Br$ as the templating agent.[11] The surfactant template in the as-synthesized material was removed by calcination at 560 °C under air for 6 h. Powder XRD (*hkl* in parentheses): 2θ (deg) = 2.51 (100), 4.33 (110), 4.97 (200), 6.55 (210); $a = 2d_{100}/\sqrt{3} = 40.6$ Å.

[NBu$_4$][Eu(NTA)$_4$] (1). A solution of 1 M NaOH (10.9 mL) was added to a solution of HNTA (2.90 g, 10.9 mmol) in EtOH (50 mL) at room temperature. $EuCl_3 \cdot 6H_2O$ (0.80 g, 2.18 mmol) was added slowly and the mixture stirred for 4 h at 50 °C. The solvent was removed under reduced pressure and the resultant yellow residue washed with *n*-hexane. A solution of $[NBu_4]Br$ (1.05 g, 3.26 mmol) in deionized water (5 mL) and EtOH (15 mL) was then added to a solution of the yellow product in deionized water (20 mL) and EtOH (60 mL), resulting in the formation of a precipitate. After stirring the mixture for 1 h at room temperature, the solid product was filtered, washed with *n*-hexane, and dried under reduced pressure. Yield: 2.97 g (94%). Crystals of **1** suitable for X-ray diffraction were prepared by the slow diffusion of diethyl ether into a solution of the complex in THF and diglyme. Elem anal. calcd for $C_{72}H_{68}EuF_{12}NO_8$ (1455.26): C, 59.42; H, 4.71; N, 0.96. Found: C, 59.69; H, 4.68; N, 1.02. Selected IR (cm^{-1}): 2962m, 2931m, 2872m, 1616s, 1568m, 1462m, 1383m, 1293s, 1243vs, 1200s, 1181s, 1129s, 788m, 682m. Selected Raman (cm^{-1}): 3054m, 2991m, 2969m, 2935m, 2878m, 1623vs, 1598s, 1467s, 1453m, 1434m, 1386vs, 1291s, 1129m, 772s, 518m, 232m. ^{1}H NMR (300 MHz, 25 °C, CD_2Cl_2, ppm): δ 7.86−7.39 (naphthyl-H, series of overlapping broad peaks and multiplet signals), 5.06 (s, CH of β-diketone), 4.01 (m, N−CH_2), 2.15 (m, N−CH_2−CH_2), 1.94 (m, N−CH_2−CH_2−CH_2), 1.25 (t, N$(CH_2)_3CH_3$).

[C$_4$mim][Eu(NTA)$_4$] (2). A solution of 1 M NaOH (6 mL) was added to a solution of HNTA (1.53 g, 5.75 mmol) in EtOH (25 mL) at room temperature. $EuCl_3 \cdot 6H_2O$ (0.42 g, 1.15 mmol) was added slowly and the solution stirred for 4 h at 50 °C. The solvent was removed under reduced pressure and the resultant yellow residue washed with *n*-hexane. A solution of $[C_4mim]PF_6$ (0.38 mL, 1.86 mmol) in deionized water (5 mL) and EtOH (15 mL) was then added to a solution of the yellow product in deionized water (10 mL) and EtOH (30 mL), resulting in the formation of a precipitate. After stirring the mixture for 1 h at room temperature, the solid product was filtered, washed with *n*-hexane and dried under reduced pressure. Yield: 1.19 g (77%). Crystals of **2** suitable for X-ray diffraction were prepared by slow diffusion of *n*-hexane into a solution of the complex in CH_2Cl_2. Elem anal. calcd for $C_{64}H_{47}EuF_{12}N_2O_8$ (1352.01): C, 56.85; H, 3.50; N, 2.07. Found: C, 56.69; H, 3.77; N, 2.07. Selected IR (cm^{-1}): 2967m, 2932m, 1614vs, 1595s, 1570m, 1530s, 1510s, 1464m, 1294vs, 1182s, 1121s, 822m, 790m, 683m, 566m. Selected Raman (cm^{-1}): 3060s, 1630vs, 1596s, 1466vs, 1432s, 1387vs, 1354m, 1288s, 1202m, 1128m, 1019m, 771s, 721m, 517s. ^{1}H NMR (300 MHz, 25 °C, CD_2Cl_2, ppm): δ 9.66 (s, N=CH−N), 8.88 (s, N−C*H*=CH−N), 8.45 (s, N−CH_3), 8.32−7.50 (overlapping naphthyl-H and N−CH=C*H*−N), 6.62 (t, N−CH_2), 4.79 (s, CH of β-diketone), 3.14 (m, N−CH_2−CH_2), 2.08 (m, N−CH_2−CH_2−CH_2), 1.20 (t, N$(CH_2)_3CH_3$).

[C$_4$mpyr][Eu(NTA)$_4$] (3a). A solution of 1 M NaOH (3.64 mL) was added to a solution of HNTA (0.97 g, 3.64 mmol) in EtOH (20 mL) at room temperature. A suspension of $EuCl_3 \cdot 6H_2O$ (0.27 g, 0.73 mmol) in EtOH (10 mL) was then added slowly and the mixture stirred for 4 h at 50 °C. The solvent was removed under reduced pressure and the product washed with diethyl ether and *n*-hexane. A solution of $[C_4mpyr]PF_6$ (0.26 g, 1.10 mmol) in deionized water (5 mL) and EtOH (15 mL) was then added to a solution of the yellow product in deionized water (30 mL) and EtOH (100 mL), resulting in the formation of a precipitate. After stirring the mixture for 1 h at room temperature, the solid product was filtered, washed with *n*-hexane, and dried under reduced pressure. Yield: 0.83 g (83%). Elem anal. calcd for $C_{66}H_{48}EuF_{12}NO_8$ (1363.0): C, 58.16; H, 3.55; N, 1.03. Found: C, 58.08; H, 3.36; N, 1.09. Selected IR (cm^{-1}): 2967m, 2936m, 2880m, 1614vs, 1593s, 1570s, 1531s, 1513s, 1482s, 1384m, 1298vs, 1197s, 1186s, 1176s, 1132vs, 791s, 683s. Selected Raman (cm^{-1}): 3060m, 2932m, 1629vs, 1595s, 1468vs, 1431m, 1385vs, 1307s, 1294s, 1198m, 1149m, 1130m, 1019m, 770s, 724m, 517s. ^{1}H NMR (300 MHz, 25 °C, CD_2Cl_2, ppm): δ 15.2−7.50 (pyridyl-H and naphthyl-H, series of broad peaks and multiplet signals), 4.76 (s, CH of β-diketone), 3.91 (br, N−CH_2), 3.72 (s, pyridyl-CH_3), 2.62 (br, N−CH_2−CH_2), 1.71 (br, N−CH_2−CH_2−CH_2), 1.48 (t, N$(CH_2)_3CH_3$).

[C$_4$mpyr][Gd(NTA)$_4$] (3b). The gadolinium(III) analogue of **3a** was prepared as described above for **3a**, using $GdCl_3 \cdot 6H_2O$. Crystals of **3b** suitable for X-ray diffraction were prepared by slow diffusion of diethyl ether into a solution of the complex in CH_2Cl_2. The experimental powder XRD pattern of **3a** was in good agreement with that simulated from the single-crystal data for **3b**, confirming that the two compounds are isostructural.

MCM-41 Grafted with Chloropropylsilyl Groups (4). Physisorbed water was removed from calcined MCM-41 by heating at 180 °C under reduced pressure for 2 h. An excess of (3-chloropropyl)-trimethoxysilane (1.5 mL) in toluene (5 mL) was then added to a suspension of the dry MCM-41 (1.5 g) in toluene (23 mL), and the mixture stirred under reflux for 24 h. The resultant powder was filtered, washed with CH_2Cl_2 (3 × 30 mL), and dried under reduced pressure at room temperature for several hours. Elem anal. found: C, 8.62; H, 2.67%. Selected IR (cm^{-1}): 2955m, 2850m, 1237s, 1192s, 1084vs, 808s, 569w, 458s. Selected Raman (cm^{-1}): 2959s, 2916s, 2897s, 2850s, 1444m, 1270m, 650m. ^{13}C CP/MAS NMR (ppm): δ 46.1 (CH_2−Cl), 26.0 (CH_2−CH_2−CH_2), 9.3 (Si−CH_2).

MCM-41 Containing Immobilized 1-Propyl-3-methylimidazolium Chloride Groups (5). An excess of 1-methylimidazole (1 mL) was added to a suspension of material **4** (1.25 g) in toluene (20 mL) and the mixture stirred under reflux for 24 h. After filtering off the solution, the resultant solid was washed with CH_2Cl_2 (2 × 30 mL), and dried under reduced pressure at room temperature for several hours. Elem anal. found: C, 14.06; H, 3.82; N, 4.23%. Selected IR (cm^{-1}): 3111w, 2954w, 2850w, 1635m, 1237s, 1193sh, 1165s, 1083vs, 944m, 807s, 751w, 641w, 620m, 563m, 458s. Selected Raman (cm^{-1}): 3167m, 3097m, 2960vs, 2919s, 2897s, 2849m, 1566m, 1452s, 1417vs, 1388s, 1337s, 1022vs, 643w. ^{13}C CP/MAS NMR (ppm): δ 136.4 (N=*C*H−N), 123.8 (N−*C*H=CH−N), 122.4 (N−CH=*C*H−N), 51.8 (N−CH_2), 36.5 (N−CH_3), 23.9 (CH_2−*C*H_2−CH_2), 9.4 (Si−CH_2).

MCM-41 Containing Immobilized 1-Propyl-3-methylimidazolium Tetrakis(naphthoyltrifluoroacetonato)europate(III) Groups (6). A solution of 1 M NaOH (3.16 mL) was added to a solution of HNTA (0.84 g, 3.16 mmol) in EtOH (20 mL) at room temperature. A suspension of $EuCl_3 \cdot 6H_2O$

(10) Sasaki, T.; Zhong, C.; Tada, M.; Iwasawa, Y. *Chem. Commun.* **2005**, 2506–2508.

(11) Nunes, C. D.; Valente, A. A.; Pillinger, M.; Fernandes, A. C.; Romão, C. C.; Rocha, J.; Gonçalves, I. S. *J. Mater. Chem.* **2002**, *12*, 1735–1742.

(0.23 g, 0.63 mmol) in EtOH (10 mL) was then added slowly and the mixture stirred for 4 h at 50 °C. The solvent was removed under reduced pressure and the resultant yellow product washed with diethyl ether and *n*-hexane. The product was dissolved in $CHCl_3$ (10 mL) and added to a suspension of material **5** (0.35 g) in toluene (15 mL). After stirring the mixture at room temperature for 23 h, the resultant powder was filtered and washed with $CHCl_3$ (3 × 20 mL), deionized water (20 mL), ethanol (2 × 20 mL), diethyl ether (20 mL), and finally dried under reduced pressure at room temperature. Elem anal. found: C, 13.59; H, 2.90; N, 2.89; Eu, 1.42%. Selected IR (cm^{-1}): 2961vw, 1683m, 1631m, 1573w, 1383w, 1291m, 1177s, 1131s, 1075vs, 959m, 794m, 685w, 566m, 460s. Selected Raman (cm^{-1}): 3172m, 3057s, 2964s, 2923m, 2898m, 1628s, 1597m, 1576w, 1465s, 1433m, 1417w, 1384vs, 1351w, 1288m, 1224m, 1216m, 1196m, 1147m, 1126m, 1020m, 958m, 935w, 868vw, 770m, 725w, 685w, 596w, 517m, 394w, 302vw, 226w, 192w.

Single-Crystal X-Ray Diffraction. Single crystals of **1**, **2**, and **3b** were manually harvested from the crystallization vials and mounted on Hampton Research CryoLoops using FOMBLIN Y perfluoropolyether vacuum oil (LVAC 25/6) purchased from Aldrich,[12] with the help of a Stemi 2000 stereomicroscope equipped with Carl Zeiss lenses. Data were collected on a Bruker X8 Kappa APEX II CCD area-detector diffractometer (Mo Kα graphite-monochromated radiation, $\lambda = 0.71073$ Å) controlled by the APEX2 software package[13] and equipped with an Oxford Cryosystems Series 700 cryostream monitored remotely using the software interface Cryopad.[14] Images were processed using the software package SAINT+,[15] and data were corrected for absorption by the multiscan semiempirical method implemented in SADABS.[16] The structures were solved using the Patterson synthesis algorithm implemented in SHELXS-97,[17,18] which allowed the immediate location of the Ln^{3+} metallic centers. All remaining non-hydrogen atoms were located from difference Fourier maps calculated from successive full-matrix least-squares refinement cycles on F^2 using SHELXL-97.[17,19] With the exception of some carbon atoms in compound **3b** (see details below), all non-hydrogen atoms were successfully refined using anisotropic displacement parameters.

The $[C_4mim]^+$ and $[C_4mpyr]^+$ organic cations in **2** and **3b** were found to be affected by structural disorder. For **2**, the terminal $-CH_2-CH_3$ group of the butyl chain was located over two distinct crystallographic positions with refined partial occupancies of ca. 78:22%. All carbon atoms refined successfully using anisotropic displacement parameters, and the C−C bond lengths for the disordered section of the chain were restrained to common refineable values (one for each part). For **3b**, the entire butyl chain was found to be structurally disordered with the partial occupancies of the two distinct crystallographic positions refining to ca. 56:44%. All C−C and C−C−C bond lengths and angles of these disordered chains were constrained to common values [1.55(1) and 2.47(1) Å for the direct C−C connections and the C···C distance along the chain, respectively] in order to ensure chemically feasible geometries for these chemical moieties. The carbon atoms composing these disordered chains in **3b** could not be refined using anisotropic displacement parameters, and a common refineable isotropic thermal parameter was employed instead.

The single crystals of **3b** were systematically isolated as very thin and long needles which diffracted very weakly, especially at high angles, even for long exposure times per acquired frame. As a consequence, even when a 0.87 Å resolution cutoff was applied, the average I/σ value remained very low (2.53), ultimately resulting in a high R merging value (Table 1). Collection of higher-angle data is only likely to be possible using synchrotron radiation or perhaps a rotating-anode source. Nevertheless, a complete data set was collected up to 24.11°, and a chemically feasible structural model could be refined.

Hydrogen atoms bound to carbon were located at their idealized positions using appropriate *HFIX* instructions in SHELXL (43 for the aromatic and the conjugated carbon atoms belonging to the β-diketonate groups, 23 for the $-CH_2-$ moieties, and 137 for the terminal methyl groups) and included in subsequent refinement cycles in riding-motion approximation with isotropic thermal displacements parameters (U_{iso}) fixed at 1.2 (for the former families of hydrogen atoms) or 1.5 (for the methyl moieties) times U_{eq} of the carbon atom to which they were attached. The last difference Fourier map synthesis showed, for **1**, the highest peak (0.641 $eÅ^{-3}$) and deepest hole (−1.050 $eÅ^{-3}$) located at 0.31 Å from H(14) and 1.19 Å from O(2); for **2**, the highest peak (1.527 $eÅ^{-3}$) and deepest hole (−1.973 $eÅ^{-3}$) located at 0.88 Å and 0.79 Å from Eu(1); and for **3b**, the highest peak (0.867 $eÅ^{-3}$) and deepest hole (−1.579 $eÅ^{-3}$) located at 1.65 Å from C(30) and 0.04 Å from Gd (1). Information concerning crystallographic data collection and structure refinement details is summarized in Table 1.

Crystallographic data (excluding structure factors) for the structures reported in this paper have been deposited with the Cambridge Crystallographic Data Centre as supplementary publication numbers CCDC-679355 (for **1**), CCDC-679356 (for **2**), and CCDC-679357 (for **3b**). Copies of the data can be obtained free of charge on application to CCDC, 12 Union Road, Cambridge CB2 2EZ, U.K. (Fax: (+44) 1223 336033. E-mail: deposit@ccdc.cam.ac.uk).

Results and Discussion

Preparation and Thermal Properties of the Complexes. Complexes **1**, **2**, **3a**, and **3b** (Chart 1) were prepared by the addition of a slight excess of $[NBu_4]Br$, $[C_4mim]PF_6$, or $[C_4mpyr]PF_6$ in ethanol/water to a solution of $Na[Ln(NTA)_4]$ (Ln = Eu, Gd) in ethanol/water. All four complexes are soluble in chlorinated solvents and polar solvents and insoluble in *n*-hexane. The solubility in diethyl ether decreases in the order **1** > **2** > **3a**/**3b**, with complex **1** being soluble and complexes **3a** and **3b** being insoluble. The thermal behavior of the europium(III) compounds was examined by DSC and TGA. DSC indicated melting points of 197 °C for **1**, 150 °C for **2**, and 200 °C for **3a**. A typical TGA trace is shown in Figure 1 for the 1-butyl-3-methylimidazolium salt (**2**). All three compounds decompose in two main steps up to 700 °C, with the onset of decomposition being in the range 225−250 °C. The first step (up to ca. 350 °C) comprises an abrupt weight loss of 67% for **1**, 48% for **2**, and 58% for **3a**. The second weight loss event occurs in the range 465−550 °C for **1**, 480−680 °C for **2**, and 460−560 °C for **3a**, leaving residual masses of 15%, 14%, and 20%, respectively.

Crystal Structure Description of 1, 2, and 3b. The structural feature common to the three crystal structures determined for $[NBu_4][Eu(NTA)_4]$ (**1**), $[C_4mim][Eu(NTA)_4]$ (**2**), and $[C_4mpyr][Gd(NTA)_4]$ (**3b**) is the presence of anionic $[Ln(NTA)_4]^-$ complexes, which

(12) Kottke, T.; Stalke, D. *J. Appl. Crystallogr.* **1993**, *26*, 615–619.
(13) *APEX2* version 2.1-RC13; Bruker AXS: Delft, The Netherlands, **2006**.
(14) *Cryopad, Remote Monitoring and Control*, version 1.451; Oxford Cryosystems: Oxford, United Kingdom, **2006**.
(15) *SAINT+ Data Integration Engine*, version 7.23a; Bruker AXS: Madison, WI, **2005**.
(16) Sheldrick, G. M. *SADABS*, version 2.01; Bruker AXS: Madison, WI, **1998**.
(17) Sheldrick, G. M. *Acta Crystallogr., Sect. A* **2008**, *64*, 112.
(18) Sheldrick, G. M. *SHELXS-97*; University of Göttingen: Göttingen, Germany, **1997**.
(19) Sheldrick, G. M. *SHELXL-97*; University of Göttingen: Göttingen, Germany, **1997**.

Table 1. Crystal and Structure Refinement Data for $[NBu_4][Eu(NTA)_4]$ (**1**), $[C_4mim][Eu(NTA)_4]$ (**2**), and $[C_4mpyr][Gd(NTA)_4]$ (**3b**)

	1	**2**	**3b**
formula	$C_{72}H_{68}EuF_{12}NO_8$	$C_{64}H_{47}EuF_{12}N_2O_8$	$C_{66}H_{48}F_{12}GdNO_8$
fw	1455.23	1352.00	1368.30
cryst syst	tetragonal	monoclinic	monoclinic
space group	$P4_2/n$ (no. 86)	$P2_1/c$ (no. 14)	$P2_1/c$ (no. 14)
temperature/K	150(2)	100(2)	180(2)
a/Å	12.6389(4)	12.6037(9)	12.664(3)
b/Å	12.6389(4)	18.8339(14)	19.393(4)
c/Å	20.7995(16)	24.5180(16)	24.432(6)
β/deg		102.494(4)	102.354(8)
volume/Å^3	3322.5(3)	5682.2(7)	5862(2)
Z	2	4	4
D_c/g cm^{-3}	1.455	1.580	1.550
μ(Mo Kα)/mm^{-1}	1.033	1.203	1.227
cryst size/mm	0.15 × 0.10 × 0.01	0.16 × 0.08 × 0.04	0.16 × 0.02 × 0.01
cryst type	colorless plates	colorless plates	colorless needles
θ range	3.72 to 27.48	3.57 to 30.10	3.53 to 24.11
index ranges	$-16 \le h \le 14$	$-17 \le h \le 17$	$-14 \le h \le 14$
	$-16 \le k \le 15$	$-26 \le k \le 22$	$-22 \le k \le 18$
	$-26 \le l \le 27$	$-34 \le l \le 34$	$-28 \le l \le 27$
reflns collected	41366	54559	72297
independent reflns	3777 (R_{int} = 0.1291)	16249 (R_{int} = 0.0451)	9125 (R_{int} = 0.2461)
data completeness	up to θ = 27.48°, 98.7%	up to θ = 30.10°, 97.2%	up to θ = 24.11°, 97.9%
final R indices [$I > 2\sigma(I)$][a,b]	R1 = 0.0807	R1 = 0.0391	R1 = 0.0600
	wR2 = 0.1615	wR2 = 0.0826	wR2 = 0.0974
final R indices (all data)[a,b]	R1 = 0.1338	R1 = 0.0682	R1 = 0.2045
	wR2 = 0.1726	wR2 = 0.0936	wR2 = 0.1367
weighting scheme[c]	m = 0.0	m = 0.0404	m = 0.0484
	n = 27.76803	n = 4.6619	n = 0.0
largest diff. peak and hole	0.641 and −1.050 eÅ^3	1.527 and −1.973 eÅ^3	0.867 and −1.579 eÅ^3

[a] $R1 = \sum||F_o| - |F_c||/\sum|F_o|$. [b] $wR2 = \sqrt{\sum[w(F_o^2 - F_c^2)^2]/\sum[w(F_o^2)^2]}$. [c] $w = 1/[\sigma^2(F_o^2) + (mP)^2 + nP]$ where $P = (F_o^2 + 2F_c^2)/3$.

Chart 1

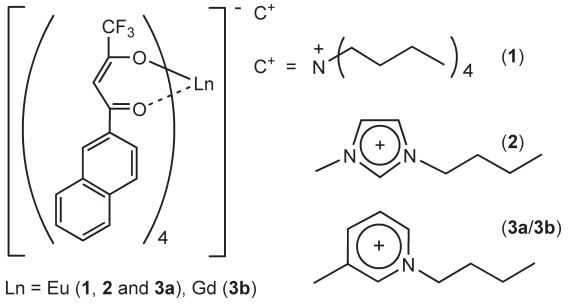

all differ according to their individual molecular geometries, as represented in Figure 2. In all compounds, the anionic NTA^- residues appear *O*,*O*-chelated to the central lanthanide centers via the ketone functional groups, leading to the formation of six-membered rings subtending an average bite angle of about 71.1° (for the three structures). This angle is in very good agreement with the analogous values found in the known Ln/NTA complexes (range 68.8−74.4° with an average bite angle of ca. 71.1°)[20] and also agrees well with those encountered

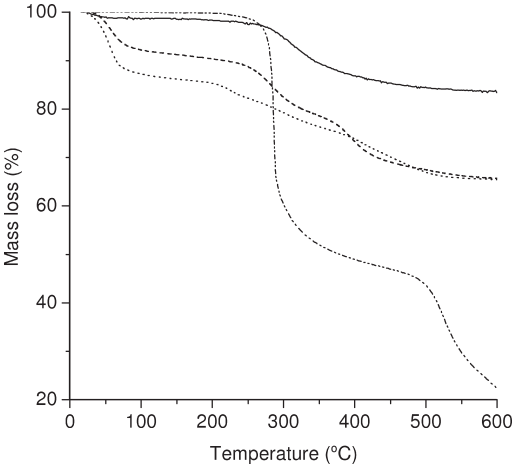

Figure 1. TGA curves of complex **2** (−··−), and materials **4** (——), **5** (− − − −) **and 6** (·····).

for Ln/BTA (BTA = benzoyltrifluoroacetonate) compounds (range 67.5−76.2° with an average bite angle of ca. 71.0°).[21] In **2** and **3b**, the O(3)−Ln(1)−O(4) bite angles [72.12(7)° and 71.8(2)°, respectively] are

(20) (a) Fernandes, J. A.; Braga, S. S.; Pillinger, M.; Ferreira, R. A. S.; Carlos, L. D.; Hazell, A.; Ribeiro-Claro, P.; Gonçalves, I. S. *Polyhedron* **2006**, *25*, 1471–1476. (b) Fernandes, J. A.; Ferreira, R. A. S.; Pillinger, M.; Carlos, L. D.; Jepsen, J.; Hazell, A.; Ribeiro-Claro, P.; Gonçalves, I. S. *J. Lumin.* **2005**, *113*, 50–63. (c) Yu, J. B.; Zhang, H. J.; Fu, L. S.; Deng, R. P.; Zhou, L.; Li, H. R.; Liu, F. Y.; Fu, H. L. *Inorg. Chem. Commun.* **2003**, *6*, 852–854. (d) Thompson, L. C.; Atchison, F. W.; Young, V. G. *J. Alloys Compd.* **1998**, *277*, 765–768. (e) Shen, F. R.; Xie, M. H.; Hu, J. P.; Wang, S. A.; Huang, X. Y. *Polyhedron* **1996**, *15*, 1151–1155. (f) Shen, F. R.; Hu, J. P.; Xie, M. H.; Wang, S. W.; Huang, X. Y. *J. Organomet. Chem.* **1995**, *485*, C6–C9. (g) Dearie, C. M.; Dyson, R. M.; Hambley, T. W.; Lawrance, G. A.; Maeder, M.; Tannock, G. A. *Aust. J. Chem.* **1993**, *46*, 577–582.

(21) (a) De Silva, C. R.; Maeyer, J. R.; Dawson, A.; Zheng, Z. P. *Polyhedron* **2007**, *26*, 1229–1238. (b) Yang, Y. T.; Driesen, K.; Nockemann, P.; Van Hecke, K.; Van Meervelt, L.; Binnemans, K. *Chem. Mater.* **2006**, *18*, 3698–3704. (c) Ma, S. L.; Qi, C. M.; Guo, Q. L.; Zhao, M. X. *J. Mol. Struct.* **2005**, *738*, 99–104. (d) Shavaleev, N. M.; Moorcraft, L. P.; Pope, S. J. A.; Bell, Z. R.; Faulkner, S.; Ward, M. D. *Chem.—Eur. J.* **2003**, *9*, 5283–5291. (e) Ma, S. L.; Zhu, W. X.; Huang, G. H.; Yuan, D. Q.; Yan, X. *J. Mol. Struct.* **2003**, *646*, 89–94. (f) Batista, H. J.; de Andrade, A. V. M.; Longo, R. L.; Simas, A. M.; de Sa, G. F.; Ito, N. K.; Thompson, L. C. *Inorg. Chem.* **1998**, *37*, 3542–3547. (g) VanMeervelt, L.; Froyen, A.; Dolieslager, W.; Walrand-Gorller, C.; Drisque, I.; King, G. S. D.; Maes, S.; Lenstra, A. T. H. *Bull. Soc. Chim. Belg.* **1996**, *105*, 377–381.

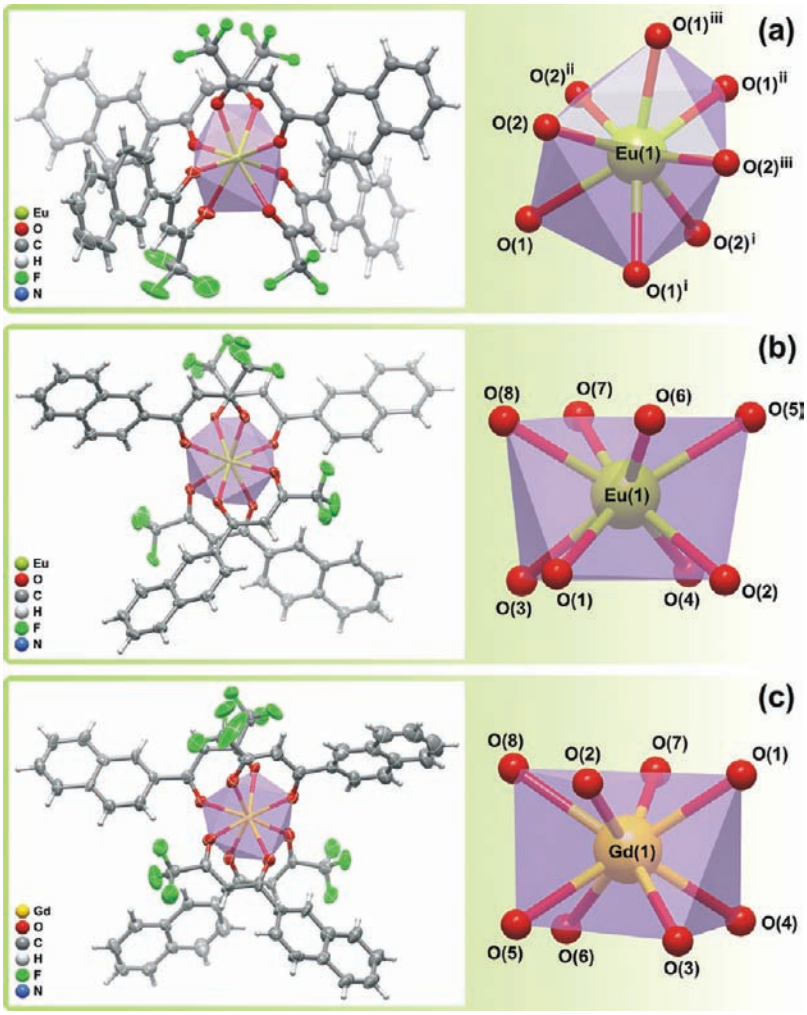

Figure 2. Schematic representation of the anionic $[Ln(NTA)_4]^-$ complexes and the respective $\{LnO_8\}$ coordination environments present in (a) $[NBu_4][Eu(NTA)_4]$ (**1**), (b) $[C_4mim][Eu(NTA)_4]$ (**2**), and (c) $[C_4mpyr][Gd(NTA)_4]$ (**3b**). Non-hydrogen atoms composing the asymmetric units are represented as thermal ellipsoids drawn at the 70% probability level, and hydrogen atoms are drawn as small spheres with arbitrary radii. The labeling scheme is provided for the atoms composing the first coordination sphere of the $\{LnO_8\}$ coordination polyhedra. Symmetry transformations used to generate equivalent atoms: (i) $1.5 - x, 1.5 - y, z$; (ii) $1.5 - y, x, 1.5 - z$; (iii) $y, 1.5 - x, 1.5 - z$. For selected bond lengths and angles, see Tables S1−S3 in the Supporting Information.

statistically distinct from the remaining angles for each structure. This structural feature can be explained by the structural stress imposed on the coordinated NTA^- residue by the close proximity of the CF_3 group with neighboring highly disordered alkyl chains of the $[C_4mim]^+$ and $[C_4mpyr]^+$ organic species (see below for a description of the crystal packing features).

The presence of $[NBu_4]^+$ cations in **1** leads to a remarkably distinct molecular geometry for the $[Eu(NTA)_4]^-$ complex when compared with **2** and **3b**. Indeed, in **1**, the Eu^{3+} center is located at the 4-fold inversion axis with only one crystallographically independent NTA^- residue composing the coordination environment (Figure 2a). The $\{EuO_8\}$ coordination sphere is thus best described as a distorted dodecahedron with the Eu−O bond distances being either 2.348(5) or 2.426(5) Å (Table S1 in the Supporting Information). Individual $[Eu(NTA)_4]^-$ complexes close-pack in the *ab* plane of the unit cell, mediated by strong offset $\pi-\pi$ interactions between NTA^- moieties belonging to neighboring complexes (Figure 3a): adjacent planar naphthyl rings (mean deviation of 0.015 Å) are separated by 3.45 Å, with the average mean planes being mutually inclined by ca. 5.5°. This supramolecular arrangement of anionic complexes leads to the formation of layers having perfectly square apertures which house the charge-balancing $[NBu_4]^+$ cations (Figure 3a). Besides electrostatic interactions, these cations are further involved in additional C−H···π contacts with neighboring naphthyl aromatic rings (not shown). Neutral layers close-pack along the [001] direction of the unit cell in an ABAB··· fashion, with the B layer being related to the A layer by 4-fold inversion symmetry (Figure 3b).

The presence of the organic cations $[C_4mim]^+$ in **2** and $[C_4mpyr]^+$ in **3b** leads to low-symmetry structures in which the entire anionic $[Ln(NTA)_4]^-$ complexes are included in the respective asymmetric units, as depicted in Figure 2b and c. The crystallographically independent Ln^{3+} centers are, therefore, coordinated to four distinct NTA^- residues in typical eight-coordinate environments, $\{LnO_8\}$, whose coordination geometries resemble slightly distorted square antiprisms. For **2**, the opposite faces of the polyhedron are defined by O(1)···O(2)···O(3)···O(4) and O(5)···O(6)···O(7)···O(8), with mean deviations of 0.062 and 0.011 Å, respectively (Figure 2b). For **3b**, the analogous faces are instead defined by O(1)···O

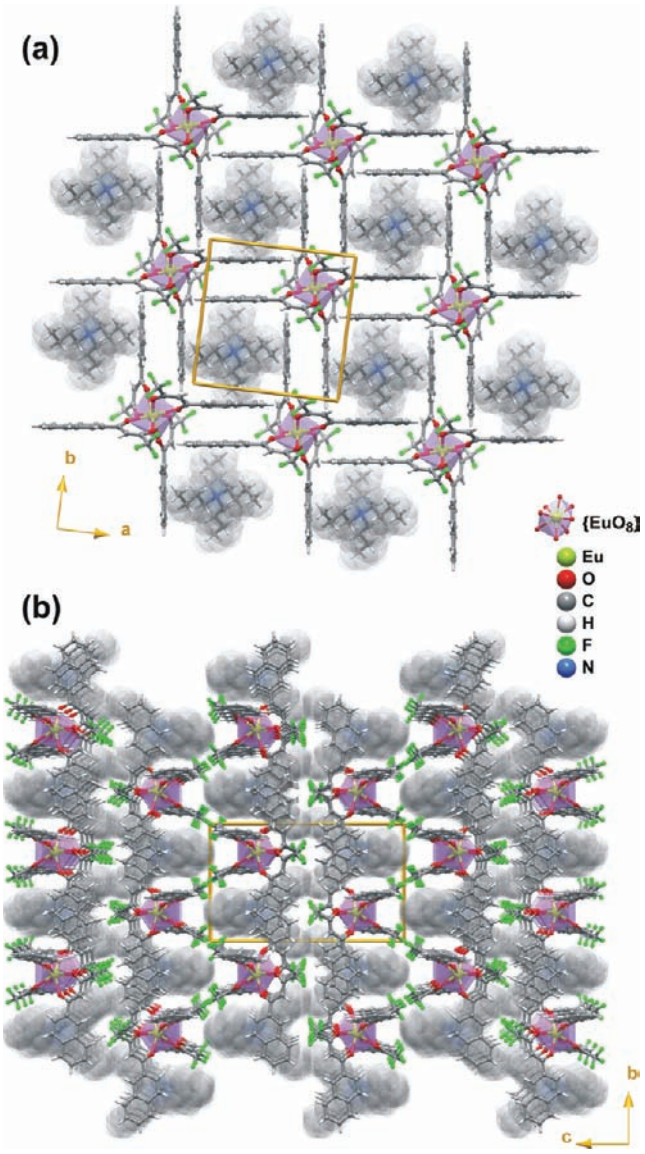

Figure 3. (a) Schematic representation of the parallel packing of [Eu(NTA)$_4$]$^-$ anionic complexes in the *ab* plane of the unit cell in [NBu$_4$][Eu(NTA)$_4$] (**1**) (mediated via $\pi-\pi$ interactions between neighboring NTA$^-$ ligands), leading to the formation of square pores which house the NBu$_4^+$ cations. (b) Perspective view of the crystal packing of **1** viewed in perspective along the [100] direction of the unit cell, emphasizing the ABAB$\cdots$ alternation along the *c* axis of layers of [Eu(NTA)$_4$]$^-$ anions. NTA$^-$ ligands are represented in ball-and-stick mode, the {EuO$_8$} coordination environments as slightly distorted dodecahedra, and NBu$_4^+$ cations in the space-filling mode.

(2)$\cdots$O(7)$\cdots$O(8) and O(3)$\cdots$O(4)$\cdots$O(5)$\cdots$O(6) with mean deviations of 0.056 and 0.100 Å, respectively (Figure 2c). In an ideal square antiprismatic environment (D_{4d} symmetry), the distribution of atoms among these two faces would describe two planes perfectly parallel to each other. The mean deviations registered for the {LnO$_8$} polyhedra clearly indicate that the diagonals of the faces are slightly creased, in particular, for the {GdO$_8$} environment in **3b** (Figure 2c). Nevertheless, the mean planes of each pair of opposite faces are still notably parallel to each other in both compounds. The observed Eu−O [range: 2.3594(19)−2.411(2) Å, Table S2 (Supporting Information)] and Gd−O [range: 2.350(6)−2.401(6) Å, Table S3 (Supporting Information)] bond distances for the {LnO$_8$} coordination antiprisms in **2** and **3b** are in accord with the geometrical parameters reported for analogous compounds with *O*,*O*-chelating β-diketonates: for Eu^{3+}, Eu−O bond distances are usually found in the 2.25−2.52 Å range (from 96 entries with a median of 2.37 Å), while for Gd^{3+}, the range is 2.26−2.47 Å (from 59 entries with a median of 2.37 Å).

The crystal packing features of **2** and **3b** are notably distinct from those of **1**. Even though the packing of neighboring lanthanide complexes is still mediated by offset $\pi-\pi$ interactions involving NTA$^-$ *O*,*O*-chelated residues and a number of weak C−H$\cdots\pi$ interactions (not shown), ultimately leading to three-dimensional supramolecular structures having empty channels running parallel to the [100] direction of the unit cell (bottom of Figures 4 and 5), the [C$_4$mim]$^+$ and [C$_4$mpyr]$^+$ chemical species are actively engaged in offset $\pi-\pi$ interactions with [Eu(NTA)$_4$]$^-$ and [Gd(NTA)$_4$]$^-$. In fact, these cations are structurally positioned along the aforementioned channels, with the imidazolium and pyridinium rings stacked between two neighboring NTA$^-$ *O*,*O*-chelated residues from distinct lanthanide complexes, with average distances between centroids of about 3.4 and 3.5 Å for **2** and **3b**, respectively (top right of Figures 4 and 5). The structural importance of these supramolecular "sandwich"-type motifs can be indirectly detected in the structural features observed for [C$_4$mim]$^+$ and [C$_4$mpyr]$^+$: even though the two rings are affected by some degree of thermal disorder, ultimately noticeable in the large magnitude of some thermal ellipsoids, their position is significantly more stagnant in the structures than those of the butyl chain substituents which were found to be severely disordered, particularly in **3b**, for which the partition between the two crystallographic positions is 56:44% (top left of Figures 4 and 5). Indeed, the possible C−H$\cdots$(π,F) interactions in which these terminal chains could be involved are significantly weaker than the offset $\pi-\pi$ stacking involving the rings, hence, the extensive disorder observed for these two species. This kind of disorder of the butyl chains is not unprecedented and has already been documented in a number of known structures having [C$_4$mim]$^+$.[22]

Preparation of the Materials. The ordered mesoporous silica MCM-41 was derivatized with 1-propyl-3-methylimidazolium groups by using a stepwise grafting procedure (Scheme 1). In the first step, calcined and dehydrated MCM-41 was treated with a toluene solution of (3-chloropropyl)trimethoxysilane under reflux to give material **4** with surface-bound chloropropylsilyl groups. Elemental analysis indicated a carbon content of 8.62%, which translates to a chloropropylsilyl loading of about 1.8 mmol g^{-1} if we assume that, on average, the chloropropylsilyl groups are bipodally anchored to the surface, with one residual methoxy group per Si atom. TGA of material **4** shows that the organic moieties decompose in one step between 260 and 420 °C, with a loss of 11.4% (Figure 1). The weight loss of 1.4%

(22) (a) van den Broeke, J.; Stam, M.; Lutz, M.; Kooijman, H.; Spek, A. L.; Deelman, B. J.; van Koten, G. *Eur. J. Inorg. Chem.* **2003**, 2798–2811. (b) Stenzel, O.; Raubenheimer, H. G.; Esterhuysen, C. *Dalton Trans* **2002**, 1132–1138. (c) Hasan, M.; Kozhevnikov, I. V.; Siddiqui, M. R. H.; Steiner, A.; Winterton, N. *Inorg. Chem.* **1999**, *38*, 5637–5641.

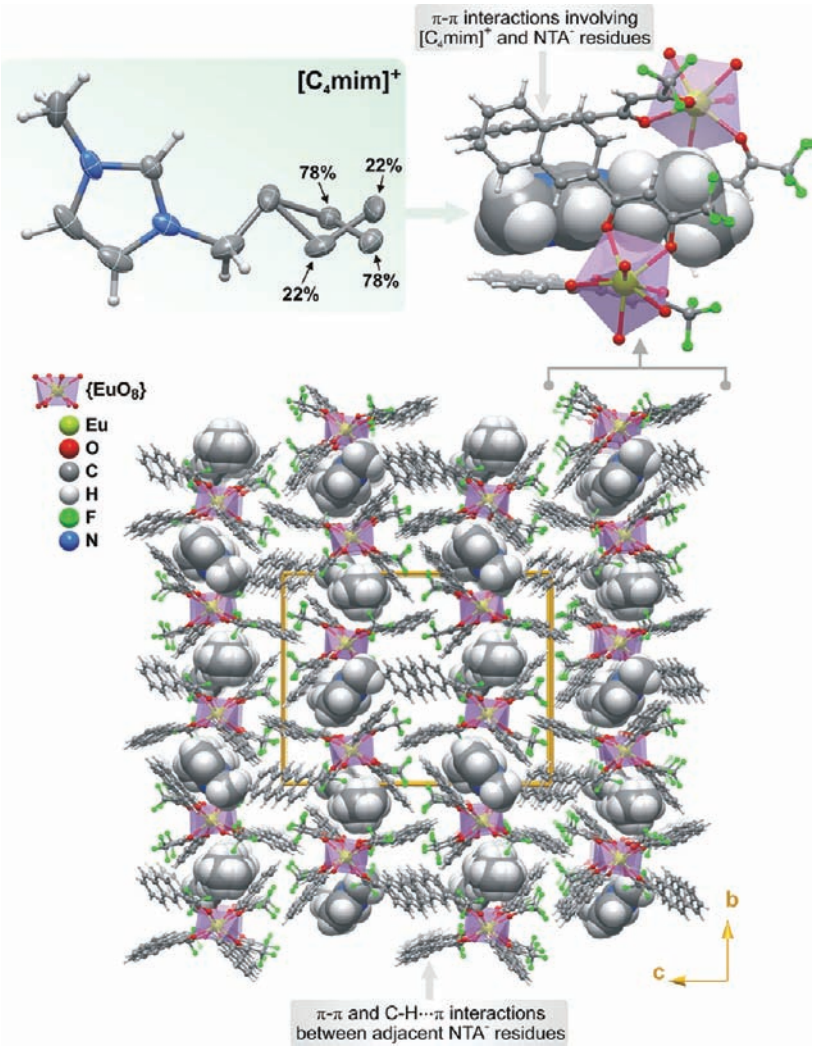

Figure 4. (Bottom) Crystal packing of $[C_4mim][Eu(NTA)_4]$ (**2**) viewed in perspective along the [100] direction of the unit cell. (Top) Schematic drawings showing the disordered $[C_4mim]^+$ cationic moiety and the "sandwich"-type supramolecular motif mediated by offset $\pi-\pi$ stacking interactions involving this cation and two neighboring $[Eu(NTA)_4]^-$ anions. NTA^- ligands are represented in ball-and-stick mode, the $\{EuO_8\}$ coordination environments as slightly distorted dodecahedra, and $[C_4mim]^+$ cations in the space-filling mode.

observed up to 100 °C is attributed to a small amount of water that was adsorbed during transfer of the sample to the TGA instrument under air.

The coupling of the imidazolium groups was performed by treatment of **4** with an excess of 1-methylimidazole in refluxing toluene. Elemental analysis of material **5** indicated a C/N molar ratio of 3.9, which is consistent with the successful derivatization of all of the bipodally anchored chloropropylsilyl groups. On the basis of the loading of 1.8 mmol g^{-1} in **4**, the theoretical C and N contents in **5** are 15.1% and 4.4%, respectively, which are slightly higher than the observed values of 14.1% and 4.2%. TGA of **5** shows an enhanced weight loss of 7.8% up to 100 °C (Figure 1), which is attributed to the fact that **5** is somewhat hygroscopic and readily adsorbs water from moist air. The water content in **5** explains the discrepancy between the experimental and theoretical elemental analysis data. Indeed, the difference between the two C contents can be accounted for by a water content of 6.9%, which is consistent with the TGA. Compared with the thermal behavior of **4**, decomposition of the organic moieties in **5** occurs over a slightly wider range (230−450 °C) and consists of two well-defined steps centered around 285 and 400 °C. The weight loss of 24.6% between 200 and 600 °C is in good agreement with the theoretical value of 26.2% calculated on the basis of a ligand loading of 1.5 mmol g^{-1} and the assumption that the organic material removed per anchored group corresponds to a formula of $C_8H_{15}N_2Cl$.

Materials **4** and **5** were further characterized by powder XRD and ^{13}C and ^{29}Si MAS NMR spectroscopy. The powder XRD pattern of material **4** is similar to that reported previously for MCM-41 derivatized with functional trialkoxysilanes (Figure 6).[9] One very intense and two very weak peaks are observed in the 2θ range 1−8°, indexed as the (100), (110), and (200) reflections of a hexagonal unit cell with d_{100} = 36.9 Å and $a = 2d_{100}/\sqrt{3}$ = 42.6 Å. After treatment with 1-methylimidazole to give material **5**, the characteristic reflections are still observed at about the same positions, demonstrating that the long-range hexagonal symmetry of the mesoporous host was preserved. The attenuation of the X-ray peaks probably arises from the presence of additional organic matter within the two-dimensional channels (rather than

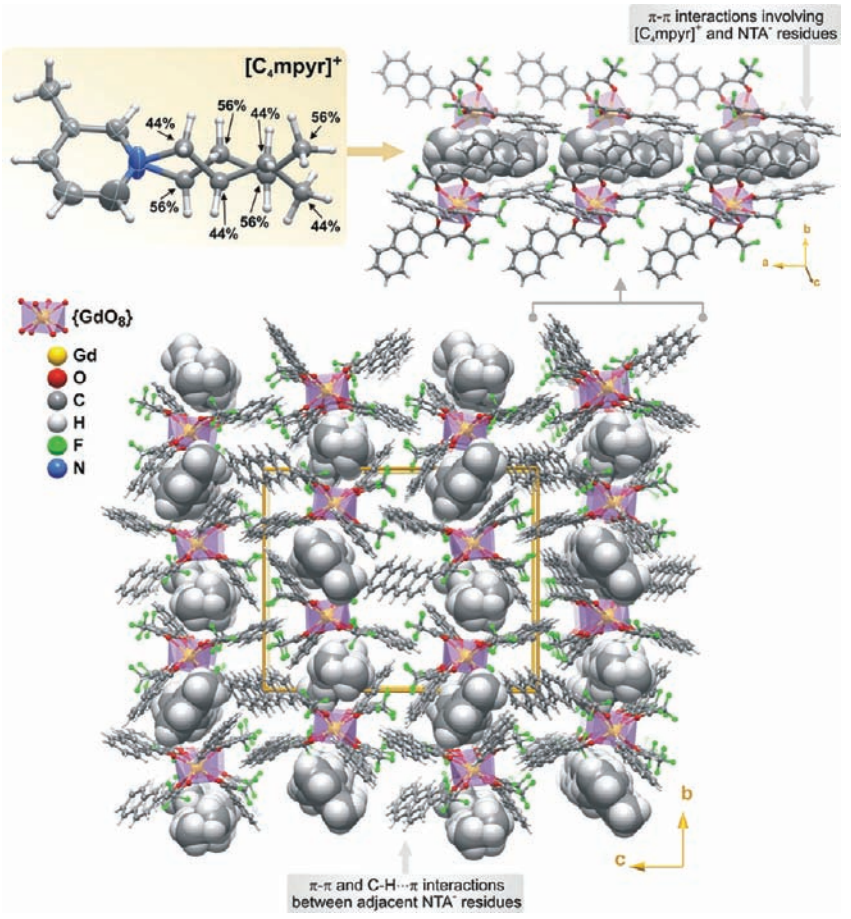

Figure 5. (Bottom) Crystal packing of $[C_4mpyr][Gd(NTA)_4]$ (**3b**) viewed in perspective along the [100] direction of the unit cell. (Top) Schematic drawings showing the disordered $[C_4mpyr]^+$ cationic moiety and the "sandwich"-type supramolecular motif mediated by offset $\pi-\pi$ stacking interactions involving this cation and two neighboring $[Gd(NTA)_4]^-$ anions. NTA^- ligands are represented in the ball-and-stick mode, the $\{GdO_8\}$ coordination environments as slightly distorted dodecahedra, and $[C_4mpyr]^+$ cations in the space-filling mode.

a loss of crystallinity), which will result in a reduction in the X-ray scattering contrast between the silica walls and pore-filling material.[9a]

The ^{13}C and ^{29}Si CP/MAS NMR spectra of the modified materials **4** and **5** provide conclusive evidence for the incorporation of the covalently linked organic systems (Figure 7). Unmodified MCM-41 displays two broad overlapping resonances at −100.8 and −107.3 ppm, assigned to Q^3 and Q^4 species of the silica framework [Q^n = $Si(OSi)_n(OH)_{4-n}$]. A weak shoulder is also observed at $\delta = -92$ ppm for the Q^2 species. Grafting of (3-chloropropyl)trimethoxysilane onto MCM-41 results in a marked decrease in the relative intensities of the Q^2 and Q^3 resonances and an increase in the intensity of Q^4. Three additional signals appear at −46.5, −57.4, and −68.7 ppm, which can be assigned to T^1, T^2, and T^3 organosilica species [T^m = $RSi(OSi)_m(OMe)_{3-m}$], respectively, with T^2 (i.e., bipodally anchored species) as the major system.

The ^{13}C CP/MAS NMR spectrum of **4** exhibits lines at 9.3, 26.0, and 46.1 for the three ^{13}C nuclei of the grafted propyl chains and no discernible peak around 50 ppm for residual methoxy groups. For material **5**, the methylene signal initially at 46.1 ppm has shifted to 51.8 ppm, which is consistent with the presence of an $N-CH_2$ unit rather than a $Cl-CH_2$ unit.[10] The presence of coupled methylimidazolium groups is confirmed by three sharp resonances in the range 122−136 ppm for the methine carbon atoms of the imidazolium ring, and a single peak at 36.5 for the methyl carbon atom. All four resonances have chemical shifts close to those exhibited by 1-(3-trimethoxysilyl)-propyl-3-methylimidazolium chloride in its solution ^{13}C NMR spectrum.[10]

Tetrakis(naphthoyltrifluoroacetonato)europate(III) complexes were immobilized in material **5** by the addition of a solution of $Na[Eu(NTA)_4]$ in $CHCl_3$ to a suspension of **5** in toluene. Elemental analysis indicated an Eu loading of about 0.1 mmol g^{-1} in material **6**, which corresponds to about 9% of the total number of anchored imidazolium groups. TGA of material **6** shows a dehydration step of 12.7% up to 100 °C (Figure 1). Decomposition of organic moieties begins at about 200 °C, and several overlapping weight loss events contribute to a combined loss of 19.9% up to 600 °C. The Raman spectrum of **6** is well-described by the sum of the spectra of **5** and $Na[Eu(NTA)_4]$, with only small frequency and intensity changes (Figure 8).

Photoluminescence Studies. Figure 9 shows the room-temperature excitation spectra of complexes **1**, **2**, and **3a** monitored within the intra-$4f^6$ $^5D_0 \rightarrow {}^7F_2$ transition. All of the spectra display a large broad band ascribed to the excited states of the ligands (260−450 nm, with three components peaking around 365, 396, and 420 nm) and the Eu^{3+} $^7F_{0,1} \rightarrow {}^5D_{1,2}$ transitions. The energy and full

Scheme 1

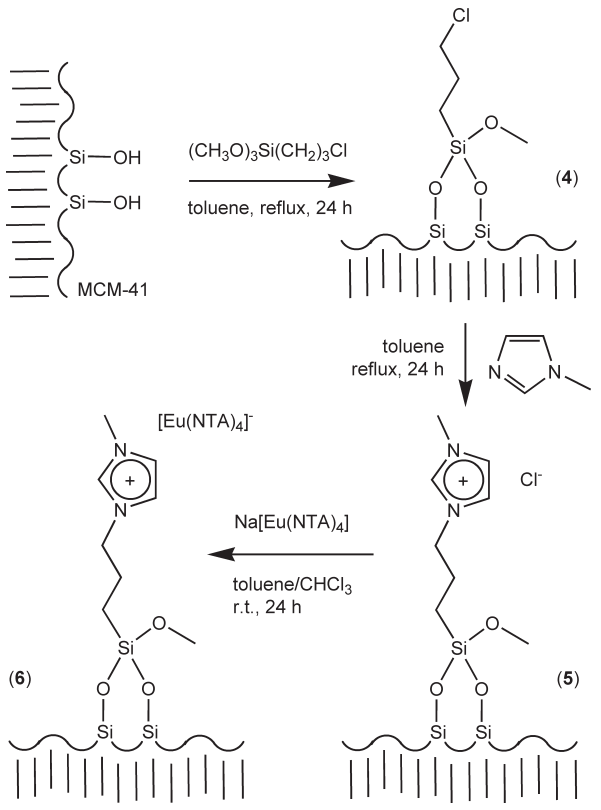

width at half-maximum (fwhm) of the broad-band components are different for each complex, showing that the counterion (C) present in the (C)[Eu(NTA)$_4$] salt influences the excitation paths of the Eu^{3+} excited levels. The relative intensity of the broad band is always higher than that of the intra-4f^6 transitions, indicating that the Eu^{3+} sensitization via the ligand's excited states is more efficient than the direct intra-4f^6 excitation. Comparing the three spectra, we may conclude that the Eu^{3+} sensitization is more efficient for complex **1** (inset of Figure 9).

Figure 10 shows the room-temperature emission spectra of the three europium(III) complexes. The spectra display the typical Eu^{3+} emission ascribed to the $^5D_0 \rightarrow {}^7F_{0-4}$ transitions. No emission from the ligand could be detected in the excitation wavelength range 280−450 nm. When the emissions of the three complexes are compared, there are differences in the energy, fwhm, relative intensity, and number of Stark components, indicating that the change in the counterion induces differences in the Eu^{3+} local symmetry, which is consistent with the single-crystal X-ray structures (especially when we compare **1** and **2**). These differences were confirmed by measuring the $^5D_0 \rightarrow {}^7F_{0-4}$ transitions with higher resolution at −259 °C, under direct intra-4f^6 excitation ($^5D_2$, 465 nm; Figure 11). Only a single line is observed for the nondegenerated $^5D_0 \rightarrow {}^7F_0$ transition (panel B in Figure 11), with a typical fwhm value of 15.0 ± 0.9 cm^{-1} for **1**, 25.2 ± 0.2 cm^{-1} for **2**, and 10.5 ± 0.1 cm^{-1} for **3a** (estimated using single Gaussian fits). The detection of a single line for the $^5D_0 \rightarrow {}^7F_0$ transition, the local-field splitting of the $^7F_{1,2}$ levels into three and four Stark components (panels C and D in Figure 11, respectively), and the higher intensity of the $^5D_0 \rightarrow {}^7F_2$ transition indicate that the Eu^{3+} local

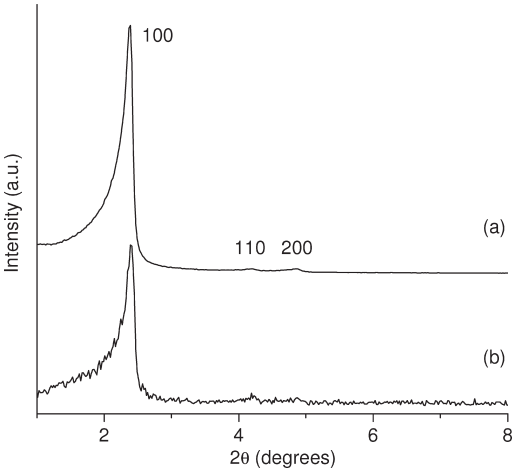

Figure 6. Powder XRD patterns of materials **4** (a) and **5** (b).

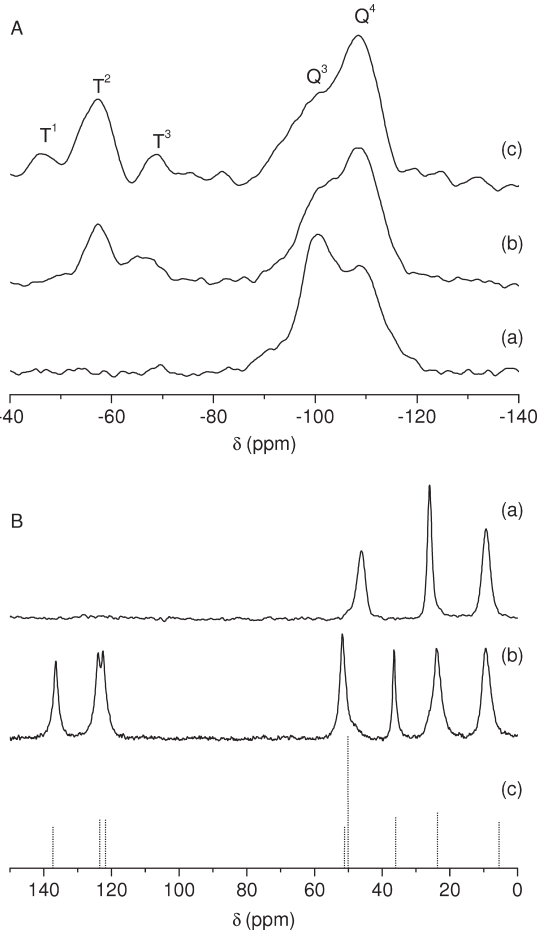

Figure 7. (A) ^{29}Si CP MAS NMR spectra of (a) MCM-41, (b) material **4**, and (c) material **5**. (B) ^{13}C CP MAS NMR spectra of (a) material **4** and (b) material **5**, compared with (c) the resonances of 1-(3-trimethoxysilyl)-propyl-3-methylimidazolium chloride in solution (dashed lines give relative intensities).

coordination site in the three complexes has a low symmetry without an inversion center. This is in agreement with the single-crystal XRD data, pointing out, for **2** and **3a**, an effective Eu^{3+} local point group of very low symmetry (C_1) and, for **1**, a dodecahedral environment with D_{2d} symmetry. Moreover, for complexes **2** and **3a**, the energy, fwhm, and relative intensity of the emission

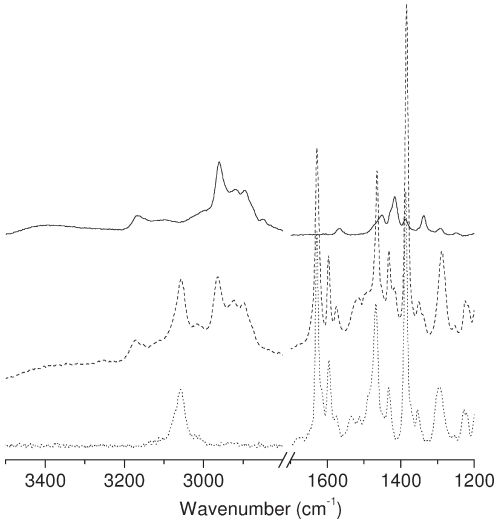

Figure 8. Two regions of the Raman spectra of material **5** (——), material **6** (– – –, and Na[Eu(NTA)$_4$] (·····).

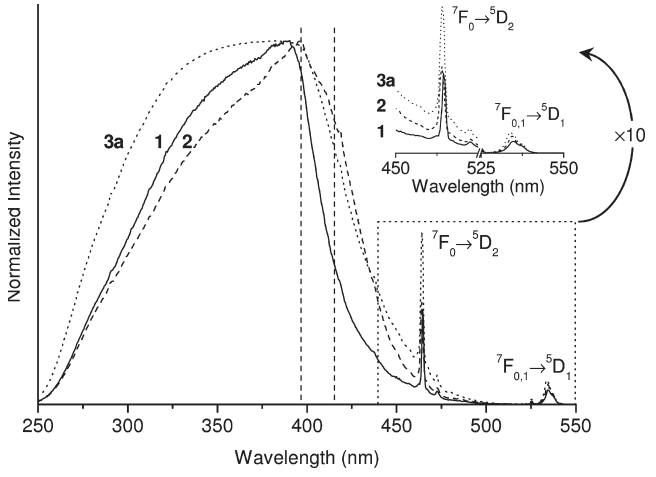

Figure 9. Room-temperature excitation spectra of complexes **1**, **2**, and **3a** monitored at 612 nm. The spectra are normalized to the broadband peak position. The inset shows a magnification of the Eu^{3+}-intra-$^4f_6$ lines.

lines are almost independent of the excitation wavelength, whereas for **1**, an increase in the fwhm and relative intensity of the Stark components is observed under excitation through ligand states (Figure S1 in the Supporting Information). Therefore, in **1**, there is a broad distribution of Eu^{3+} centers possessing slightly distinct local environments.

The $^5D_0$ emission decay curves were monitored within the $^5D_0 \rightarrow {}^7F_2$ transition under direct intra-$4f^6$ excitation ($^5D_{2,1}$, 465 and 534 nm, respectively). All of the experimental curves were well-reproduced by a single exponential function (not shown), giving lifetimes of 0.269 ± 0.001 ms for **1**, 0.559 ± 0.001 ms for **2**, and 0.693 ± 0.001 ms for **3a**. When complex **1** was excited via ligand states, minor changes were observed in the monoexponential emission decay curves (not shown), in accordance with the broad distribution of Eu^{3+} centers mentioned above. However, for complexes **2** and **3a**, for times up to ca. 0.80 ms, the $^5D_0$ decay curves are clearly nonexponential (not shown), being characterized by a rise-time branch indicating the existence of a nonradiative energy transfer process. For times above ca. 0.80 ms, the decay curves are well-fitted

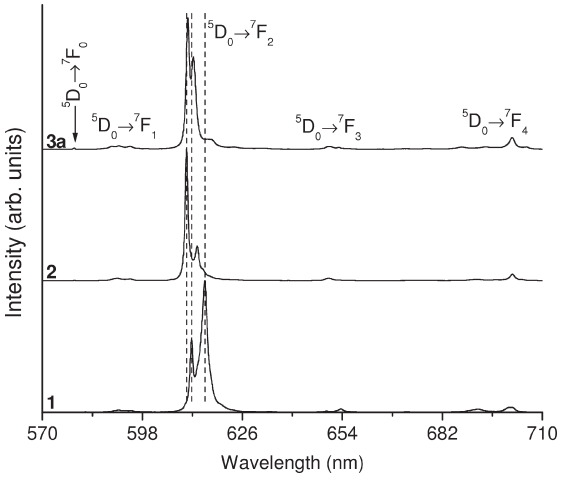

Figure 10. Room-temperature emission spectra of complexes **1**, **2**, and **3a** excited at 465 nm.

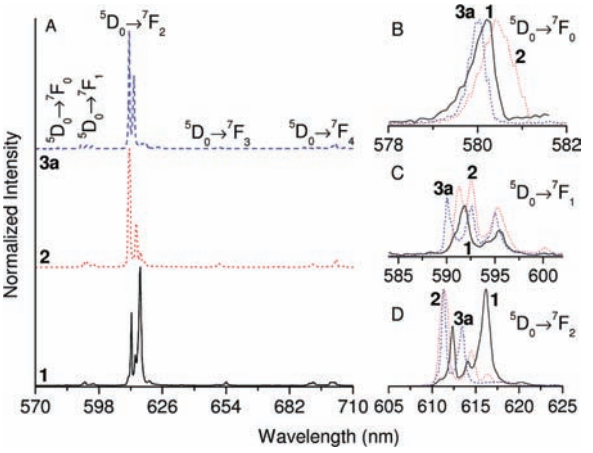

Figure 11. (A) Emission spectra of complexes **1** (solid line), **2** (dotted line), and **3a** (dashed line) acquired at −259 °C and excited at 465 nm. Insets B, C, and D show in detail the $^5D_0 \rightarrow {}^7F_{0-2}$ transitions.

with a monoexponential function giving lifetime values independent of the excitation wavelength. A detailed discussion of this process lies outside the scope of this work.

The emission features were quantified through the estimation of the $^5D_0$ radiative (k_r) and nonradiative (k_{nr}) transition probabilities and the quantum efficiency (q) [$q = k_r/(k_r + k_{nr})$], based on the emission spectrum and the $^5D_0$ lifetime values (Table 2).[1] Compound **1b** has the highest k_r and k_{nr} values, which give a q value of 0.46. The highest q value (0.56) is found for **2**, which has the lowest k_{nr} value. For complex **3a**, despite exhibiting the highest $^5D_0$ lifetime value of 0.693 ms, it has the lowest q value due to the low k_r value, as compared with those for **1** and **2**.

The emission features of the three Eu^{3+} complexes were further quantified though the measurement of the absolute emission quantum yields (ϕ) under different excitation wavelengths (Figure 12). For all three complexes, the quantum yield values under excitation via the excited states of the ligands (290 and 395 nm) are higher than those under direct intra-$4f^6$ excitation (465 and 534 nm). The quantum yield values of **1** and **3a** are approximately the same with a maximum value

Table 2. $^5D_0$ Lifetime Values (τ, ms); Experimental (k_{exp}, ms^{-1}), Radiative (k_r, ms^{-1}), and Nonradiative (k_{nr}, ms^{-1}) Transition Probabilities; and Quantum Efficiency (q) for Complexes **1**, **2**, and **3a** (λ_{exc} = 465 nm) and Material **6** (λ_{exc} = 320 nm)

	1	2	3a	6
τ	0.269 ± 0.001	0.559 ± 0.001	0.693 ± 0.001	0.626 ± 0.001
k_{exp}	3.717	1.789	1.443	1.597
k_r	1.719	0.994	0.558	0.716
k_{nr}	1.998	0.795	0.885	0.882
q	0.46	0.56	0.39	0.45

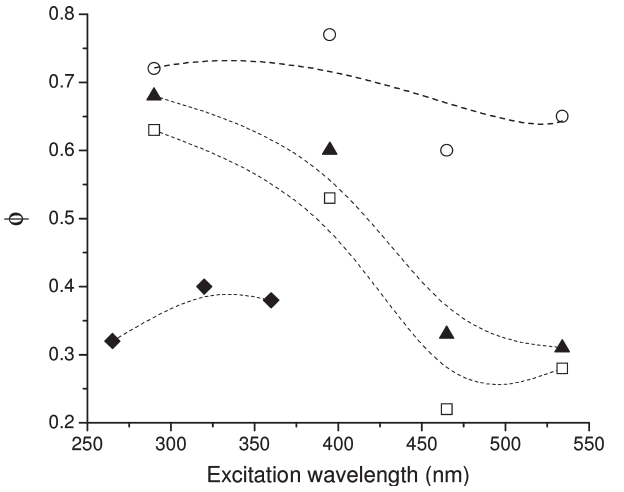

Figure 12. Absolute emission quantum yields for **1** (□), **2** (○), **3a** (▲), and **6** (♦), under different excitation wavelengths. The dotted lines are visual guides.

of 0.63−0.68 under 290 nm excitation. Complex **2** has the highest emission quantum yield of 0.77 at an excitation wavelength of 395 nm. The high quantum yield values for **2** prompted the following variable-temperature study and the preparation of an immobilized analogue of the complex.

Excitation spectra (monitored within the $^5D_0 \rightarrow {}^7F_2$ transition) were acquired for complex **2** from room temperature to 155 °C (i.e., up to the melting point; Figure 13A). The spectra were normalized to the $^7F_0 \rightarrow {}^5D_1$ transition because, due to its magnetic dipole character, it may be used as a reference in the comparison. As the temperature increases from 20 °C (Figure 9) to 130 °C (Figure 13A), there is a gradual decrease in the relative intensity of the excitation component at 365 nm (ca. 60%), whereas the component at 415 nm increases (ca. 70%), being the dominant excitation path. Near the melting point of complex **2** (ca. 155 °C), the component at 396 nm becomes the main one (as in the room-temperature excitation spectrum) due to a significant decrease (ca. 75%) in the contribution of the component at 415 nm (the relative intensity of the band at 365 nm is similar to the room-temperature value), and the spectrum resembles the room-temperature excitation spectrum of complex **1** (Figure 9). The temperature increase also leads to a more efficient sensitization process as the decrease of the relative intensity of the Eu^{3+} lines indicates.

The Eu^{3+} emission lines of complex **2** (particularly the dominant $^5D_0 \rightarrow {}^7F_2$ transition) were also monitored in the same temperature range (Figure 13B). Significant changes in the relative intensity of the high-wavelength $^7F_2$ Stark

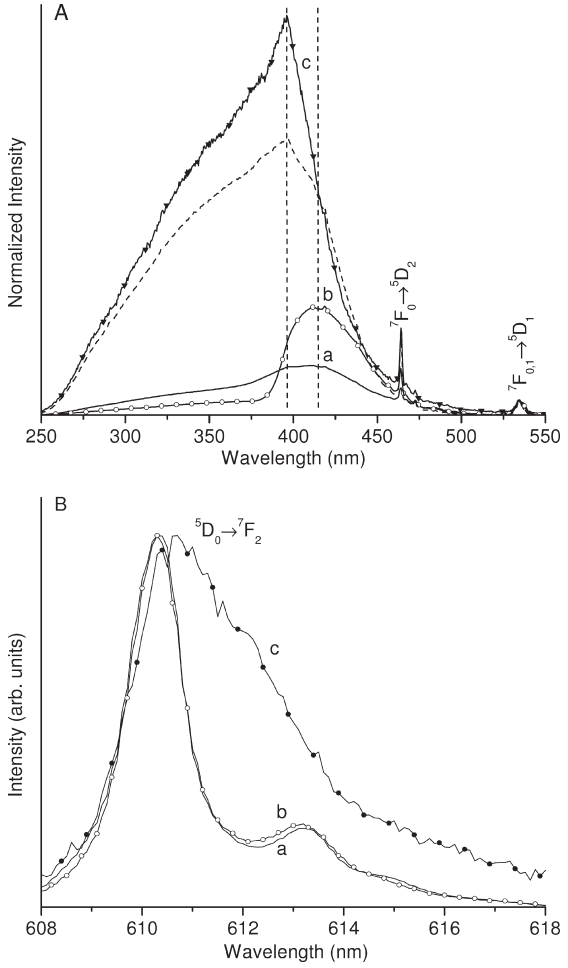

Figure 13. (A) Excitation spectra monitored at 612.0 nm and (B) $^5D_0 \rightarrow {}^7F_2$ transition excited at 396 nm for complex **2**, acquired at (a) 60 °C, (b) 130 °C, and (c) 155 °C. The dashed line is the excitation spectrum acquired at 20 °C.

components (611−615 nm) of the $^5D_0 \rightarrow {}^7F_2$ transition are evident for temperatures close to the melting point. Therefore, the alterations in the excitation and emission spectra show the ability of Eu^{3+} to act as a local probe, even for sensing well beyond the first coordination sphere.

The excitation spectrum of material **6** is shown in Figure 14. Compared with the spectrum of complex **2** (Figure 9), there is a deviation toward the blue and the Eu^{3+} intra-$4f^6$ lines disappear, pointing to an increase in the sensitization process of the Eu^{3+} ions relative to direct intra-$4f^6$ excitation. A similar phenomenon was observed for $Eu(NTA)_3$ complexes immobilized in MCM-41 functionalized with a chelating pyrazolylpyridine ligand.[9a] As found for **2**, the excitation spectrum acquired at −259 °C is essentially the same as that measured at room temperature, apart from differences in the relative intensity of the excitation components. The emission spectra of material **6**, recorded between −259 and +27 °C, are formed of the typical Eu^{3+} $^5D_0 \rightarrow {}^7F_{0-4}$ transitions, whose number of Stark components, relative intensity, energy, and fwhm do not depend significantly on the temperature (Figure 15). In particular, the $^5D_0 \rightarrow {}^7F_0$ transition peaks at 17247.3 ± 0.4 cm^{-1} with fwhm = 39.2 ± 0.8 cm^{-1} (−259 °C) and at 17246.6 ± 0.3 cm^{-1} with fwhm = 35.7 ± 0.7 cm^{-1} (27 °C).

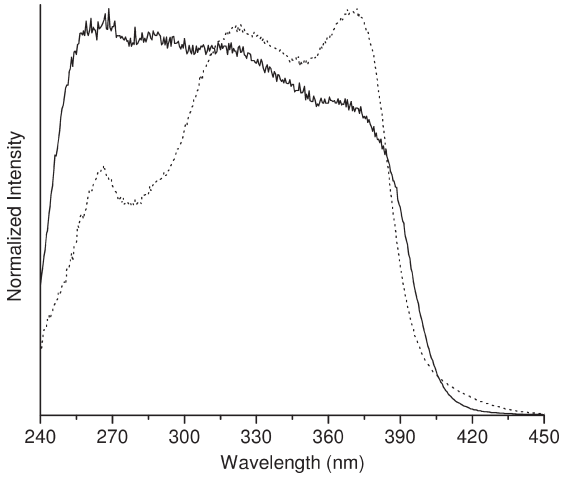

Figure 14. Excitation spectra of material **6** monitored at 612.0 nm and acquired at room temperature (solid line) and −259 °C (dotted line).

The $^5D_0$ emission decay curves were monitored within the more intense lines of the $^5D_0 \rightarrow {}^7F_2$ transition at −259 and +27 °C (not shown). At room temperature, the decay curve obtained using an excitation wavelength of 320 nm shows, for times up to ca. 0.70 ms, a rise time followed by a single exponential dependence with a lifetime value of 0.626 ± 0.001 ms. The decay curves monitored at −259 °C do not display the aforementioned rise time (a detailed discussion of which lies outside the scope of this work), being well-reproduced by a single exponential function, giving lifetime values of 0.562 ± 0.002 ms.

There are several notable differences in the photoluminescence features of complex **2** and material **6**, as exemplified by the energy and fwhm of the $^5D_0 \rightarrow {}^7F_0$ emission line (at −259 °C, $E_{00} = 17228.3 \pm 0.2$ cm^{-1} for **2** and 17247.3 ± 0.4 cm^{-1} for **6**, and fwhm = 25 cm^{-1} for **2** and 40 cm^{-1} for **6**).

The broader emission lines for the $[Eu(NTA)_4]^-$ anion immobilized in the derivatized mesoporous material point to a large distribution of Eu^{3+} centers possessing closely related local environments, and the blue shift in E_{00} in the supported material (relative to **2**) indicates a decreasing covalency of the Eu^{3+}−ligand bonds, since this transition has been related to the covalent nature of the Eu^{3+}−ligand bonds.[23,24] The energy of the $^5D_0 \rightarrow {}^7F_0$ transition is linked with the so-called *nephelauxetic* effect, in which the red shift observed for d−d and f−f energy differences, with respect to the free ion value, is associated with the increase of the covalent character of the Eu^{3+}−ligand bonds[24] (and the concomitant decrease in the values of the Slater integrals and spin−orbit coupling parameter[25]). The blue shift probably results from the interaction with the mesoporous host. A similar shift was found for Eu^{3+}-containing silica nanocomposites, where it was suggested that the complex in the nanocomposite was bound to the silica surface via silanol groups.[26]

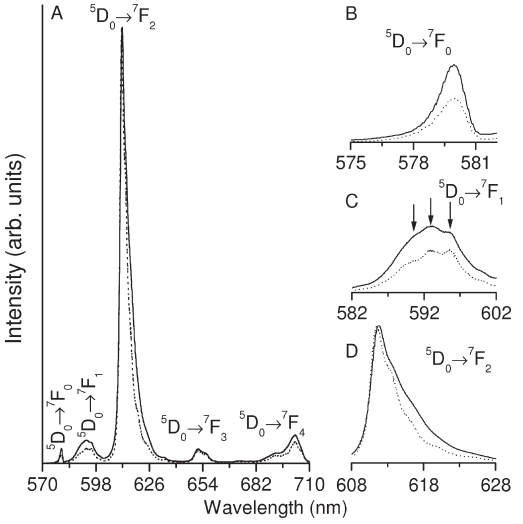

Figure 15. (A) Emission spectra of material **6** excited at 370.0 nm and acquired at room temperature (solid line) and −259 °C (dotted line). Insets B, C, and D show in detail the $^5D_0 \rightarrow {}^7F_{0-2}$ transitions.

The emission features of **6** were also quantified through the estimation of the k_r, k_{nr}, and q parameters, and the measurement of the absolute emission quantum yield (Table 2 and Figure 12). The number of reports of quantum yield measurements in lanthanide-containing mesostructured organic/inorganic hybrids is scarce,[1b,9c,27] when compared to the number of manuscripts reporting their emission features. The values of q and ϕ for **6** are similar, which indicates a rather efficient population of the $^5D_0$ excited level. Moreover, these values are the highest so far reported for lanthanide-containing ordered mesoporous silicas. Compared with complex **2**, the supported material displays smaller values of q and ϕ together with a relatively high k_{nr} value (Table 2 and Figure 12), pointing to the occurrence of more efficient nonradiative channels relative to that present in complex **2**. A similar effect has already been reported for other europium(III) β-diketonate complexes immobilized in MCM-41-derived materials,[9a,9c] and in other organic/inorganic hybrids.[1b,28]

Conclusions

In this study, it is shown that the counterion C^+, $[NBu_4]^+$, $[C_4mim]^+$, or $[C_4mpyr]^+$, present in the (C)[Eu(NTA)$_4$] salt, has a strong influence on the structure of the anion and the optical properties of powdered samples. The Eu^{3+} sensing ability can be applied to monitor the phase transition of the salt with C = $[C_4mim]^+$, particularly temperature-dependent $\pi-\pi$ interactions involving naphthyl rings of neighboring units. Under ligand excitation, the absolute emission quantum yields are in the range of 0.53−0.77, with the highest values being comparable with the maximum values previously reported for ternary complexes of the type Eu(diket)$_3$(Lig)$_n$ (e.g.,[29] $\phi = 0.75$ with diket = NTA, Lig = DMSO, and $n = 2$). Although lanthanide(III) tetrakis(β-diketonate) complexes usually show much higher luminescence intensities

(23) Frey, S. T.; Horrocks, W. D. *Inorg. Chim. Acta* **1995**, *229*, 383–390.
(24) (a) Carlos, L. D.; Malta, O. L.; Albuquerque, R. Q. *Chem. Phys. Lett.* **2005**, *415*, 238-–242. (b) Malta, O. L.; Batista, H. J.; Carlos, L. D. *Chem. Phys.* **2002**, *282*, 21–30.
(25) Carlos, L. D.; Videira, A. L. L. *J. Chem. Phys.* **1994**, *101*, 8827–8830.
(26) Soares-Santos, P. C. R.; Nogueira, H. I. S.; Félix, V.; Drew, M. G. B.; Ferreira, R. A. S.; Carlos, L. D.; Trindade, T. *Chem. Mater.* **2003**, *15*, 100–108.
(27) Zhao, D.; Seo, S.-J.; Bae, B.-S. *Adv. Mater.* **2007**, *19*, 3473–3479.
(28) Fernandes, M.; Nobre, S. S.; Gonçalves, M. C.; Charas, A.; Morgado, J.; Ferreira, R. A. S.; Carlos, L. D.; de Zea Bermudez, V. *J. Mater. Chem.* **2009**, *19*, 733–742.
(29) Carlos, V. D.; de Mello Donegá, L. D.; Albuquerque, R. Q.; Alves, S. Jr; Menezes, J. F. S.; Malta, O. L. *Mol. Phys.* **2003**, *101*, 1037–1045.

than the tris complexes, they have the disadvantage of being charged species, which can be problematic in the design of electroluminescent devices. Nevertheless, by an appropriate choice of the cation, these complexes can be used to produce luminescent ionic liquid crystals,[6] ionogels,[7] and Langmuir−Blodgett films,[1a] as well as light-emitting diodes based on doped polymer films.[1a,30] By functionalizing the ordered mesoporous silica MCM-41 with 1-propyl-3-methylimidazolium groups, we have been able to prepare an immobilized analogue of the complex $[C_4mim][Eu(NTA)_4]$ by an ion exchange route. To the best of our knowledge, this represents a novel process for the incorporation of anionic tetrakis complexes in mesostructured silica hosts; the only previous method concerns hydrogen-bonding interactions between encapsulated $(C)[Eu(TTA)_4]$ complexes and surface-modified MCM-41.[31]

Compared with $[C_4mim][Eu(NTA)_4]$, the photoluminescence features of the supported tetrakis complex point to a large distribution of Eu^{3+} centers possessing closely related local environments, and a change in the Eu^{3+} first coordination sphere toward a less covalent environment, indicating an effective host-to-Eu^{3+} interaction. Although the excitation spectrum indicates an increase in the sensitization process of the Eu^{3+} ions, relative to direct metal excitation, the absolute quantum yield under ligand excitation was lower than the maximum value found for $[C_4mim][Eu(NTA)_4]$, which is attributed to the presence of more efficient nonradiative channels in the supported material. However, despite this increase in the importance of the nonradiative paths, the quantum yield measured for **6** is the highest so far reported for lanthanide-containing ordered mesoporous silicas. We anticipate that further improvements will be possible through the passivation of residual silanol groups or the tethering of other types of organic cations.

Acknowledgment. We are grateful to the Fundação para a Ciência e a Tecnologia (FCT), the Programa Operacional Ciência e Inovação (POCI) 2010, Orçamento do Estado (OE), and Fundo Europeu de Desenvolvimento Regional (FEDER) for funding (Project POCI/CTM/58507/2004). The FCT is acknowledged for a doctoral grant to S.M.B. and for the financial support towards the purchase of the single-crystal diffractometer.

Supporting Information Available: Crystallographic information files (CIF); selected bond lengths and angles (Tables S1−S3) for the Ln^{3+} coordination environments in complexes **1**, **2**, and **3b**; and room temperature emission spectra of complexes **1**, **2**, and **3a** excited through ligand states (314−390 nm). This material is available free of charge via the Internet at http://pubs.acs.org.

(30) Yu, G.; Liu, Y.; Wu, X.; Zhu, D.; Li, H.; Jin, L.; Wang, M. *Chem. Mater*. **2000**, *12*, 2537–2541.
(31) Xu, Q.; Li, L.; Liu, X.; Xu, R. *Chem. Mater*. **2002**, *14*, 549–555.